

Supporting Information

MoS₂ Quantum Dot/Graphene Hybrids for Advanced Interface Engineering of CH₃NH₃PbI₃ Perovskite Solar Cell with Efficiency over 20%

Leyla Najafi,^{†,‡} Babak Taheri,^{#,‡} Beatriz Martín-García,[†] Sebastiano Bellani,[†] Diego Di Girolamo,[#]
Antonio Agresti,[#] Reinier Oropesa-Nuñez,^{†,||} Sara Pescetelli,[#] Luigi Vesce,[#] Emanuele Calabrò,[#]
Mirko Prato,[⊥] Antonio E. Del Rio Castillo,[†] Aldo Di Carlo,^{#,£*} Francesco Bonaccorso^{†,||*}

[†] Graphene Labs, Istituto Italiano di Tecnologia, via Morego 30, 16163 Genova, Italy.

[#] C.H.O.S.E. (Centre for Hybrid and Organic Solar Energy), Department of Electronic Engineering, University of Rome Tor Vergata, Via del Politecnico 1, Rome 00133, Italy.

^{||} BeDimensional Srl., Via Albisola 121, 16163 Genova, Italy.

[⊥] Materials Characterization Facility, Istituto Italiano di Tecnologia, via Morego 30, 16163 Genova, Italy.

[£] L.A.S.E. - Laboratory for Advanced Solar Energy, National University of Science and Technology "MISiS", 119049 Leninskiy prosect 6. Moscow, Russia.

Corresponding Author

* Tel: +39 01071781795. E-mail: francesco.bonaccorso@iit.it

Morphological analysis of MoS₂ flakes.

Figure S1 reports the morphological analysis (*i.e.*, lateral size and thickness) of the liquid phase exfoliated MoS₂ flakes, from which MoS₂ quantum dots (QDs) were derived by subsequent solvothermal treatment. Figure S1a shows a representative transmission electron microscopy (TEM) image of the MoS₂ flakes, which exhibited regular shaped borders. Figure S1b reports the statistical analysis of lateral dimension of the MoS₂ flakes, which exhibited an average lateral size of ~420 nm. Figure S1c shows a representative atomic force microscopy (AFM) image of the MoS₂ flakes. Height profiles (dashed white lines) indicated the presence of one- and two-layer flakes (the monolayer thickness is between 0.7 and 0.8 nm^{1,2}). Figure S1d shows the statistical analysis of the thickness of MoS₂ flakes, which exhibited an average thickness of ~2.7 nm.

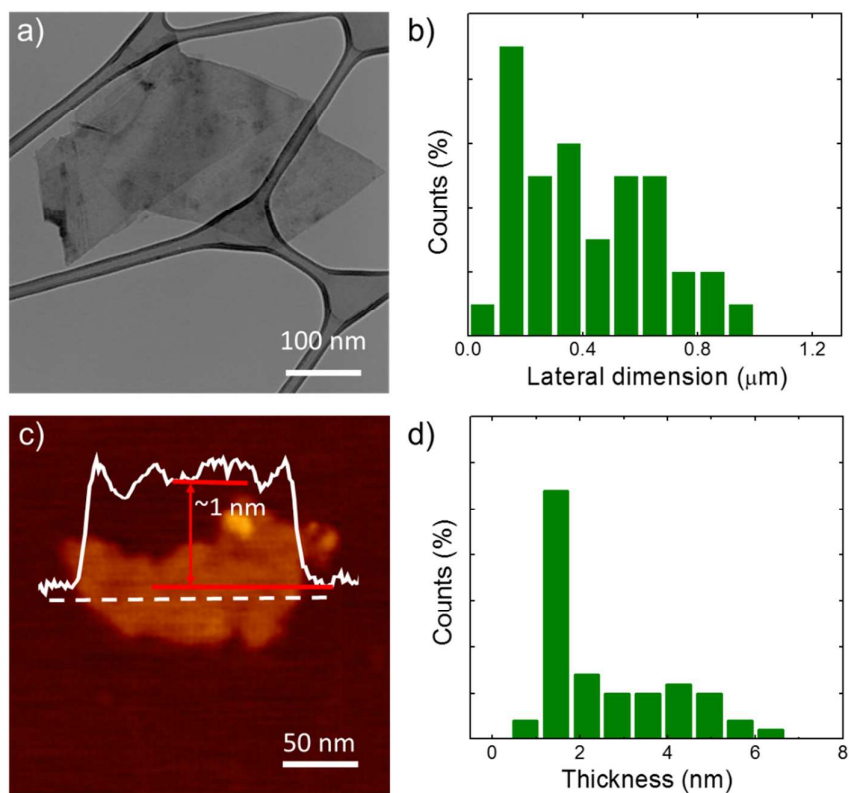


Figure S1. Morphological characterization of the as-produced MoS₂ flakes. (a) TEM image of the MoS₂ flakes. (b) Statistical analysis of the lateral dimension of the MoS₂ flakes (calculated on 100 flakes from different TEM images). (c) AFM image of the MoS₂ flakes. Representative height profile (solid white lines) of the indicated section (white dashed lines) is also shown. (d) Statistical analysis of the thickness of the MoS₂ flakes (calculated on 50 flakes from different AFM images).

Morphological analysis of RGO flakes

Figure S2 reports the morphological analysis of the as-produced reduced graphene oxide (RGO) flakes. Figure S2a shows a representative TEM image of the RGO flakes, which have an irregular shape and rippled structure. Figure S2b reports the statistical analysis of the lateral dimension of the RGO flakes, which have an average value of 1.7 μm . Figure S2c shows a representative AFM image of the RGO flakes. Height profiles (dashed white lines) evidence nano-edge steps between 0.6 and 1.6 nm. Figure S2d shows the statistical analysis of the RGO flakes, which have an average thickness of ~ 1.8 nm. This indicates that few-layer RGO flakes were effectively produced (the monolayer thickness is ~ 0.34 nm^{3,4}).

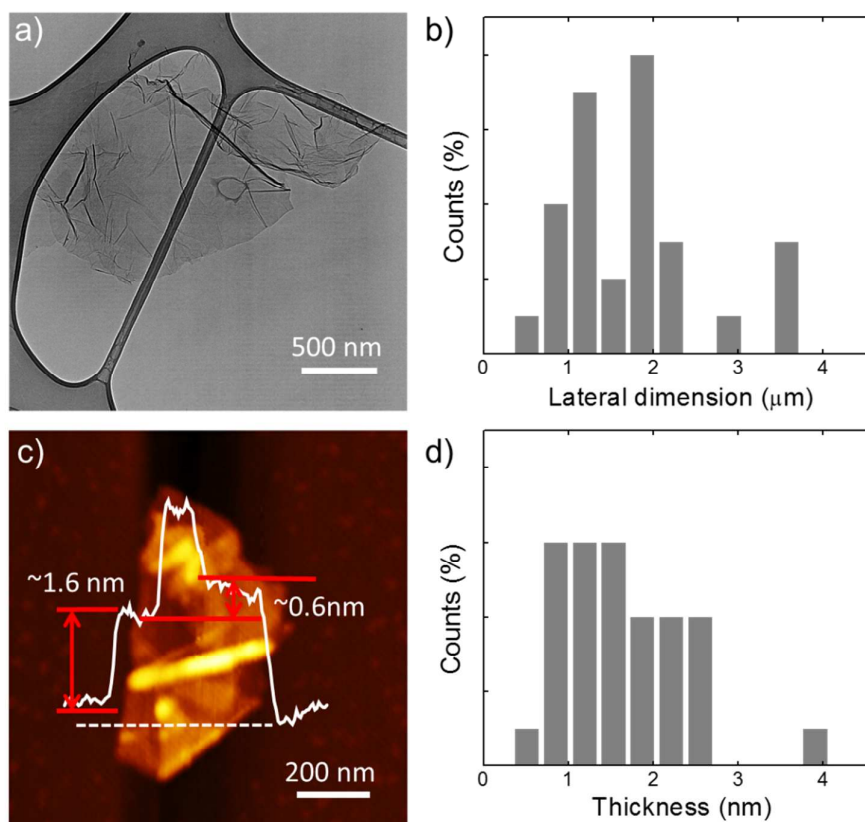


Figure S2. Morphological characterization of the as-produced RGO flakes. (a) TEM image of the RGO flakes. (b) Statistical analysis of the lateral dimension of the RGO flakes (calculated on 100 flakes from different TEM images). (c) AFM image of the RGO flakes. Representative height profile (solid white lines) of the indicated section (white dashed lines) is also shown. (d) Statistical analysis of the thickness of the RGO flakes (calculated on 50 flakes from different AFM images).

Raman spectroscopy characterization of materials

Figure S3a reports representative Raman spectra of MoS₂ QDs, compared to both native bulk MoS₂ powder and MoS₂ flakes. These spectra show the presence of first-order modes at the Brillouin zone center E_{2g}¹(Γ) (~379 cm⁻¹ for both MoS₂ flakes and QDs, and ~377 cm⁻¹ for bulk MoS₂) and A_{1g}(Γ) (~403 cm⁻¹), involving the in-plane displacement of Mo and S atoms and the out-of-plane displacement of S atoms, respectively.^{5,6} The E_{2g}¹(Γ) mode of both the MoS₂ flakes and QDs exhibits softening compared to the one of the bulk MoS₂. The shift of the E_{2g}¹(Γ) mode is explained by the dielectric screening of long-range Coulomb MoS₂ interlayer interaction.⁵ The full width at half maximum (FWHM) of the E_{2g}¹(Γ) and A_{1g}(Γ) (*i.e.*, FWHM(E_{2g}¹(Γ)) and FWHM(A_{1g}(Γ)), respectively) of both MoS₂ flakes and MoS₂ QDs increases of ~3 cm⁻¹ and ~2 cm⁻¹, respectively, compared to the corresponding modes of bulk MoS₂. The increase of FWHM(A_{1g}(Γ)) for MoS₂ flakes and MoS₂ QDs is attributed to the variation of interlayer force constants between the inner and outer layers.²

Figure S3b shows representative Raman spectra of functionalized RGO (f-RGO) flakes, together with its native materials, *i.e.*, graphene oxide (GO) and RGO flakes. The Raman spectrum of GO flakes reveals two main peaks located at 1352 and 1591 cm⁻¹, corresponding to D and G bands, respectively.^{7,8} The G peak corresponds to the E_{2g} phonon at the Brillouin zone center,^{7,8} while the D peak is due to the breathing modes of sp² rings,^{7,8} requiring a defect for its activation by double resonance.⁷ The 2D peak position, located at ~2700 cm⁻¹ is the second order of the D peak.⁹ Double resonance can also happen as an intravalley process, *i.e.*, connecting two points belonging to the same cone around K or K'.⁹ This process gives rise to the D' peak, which is usually located at ~1600 cm⁻¹ in presence of high density defects.⁹ In these conditions, the D' band is merged with the G band. The 2D' peak, located at ~3200 cm⁻¹, is the second order of the D',⁹ while D+D', positioned at ~2940 cm⁻¹ is the combination mode of D and D'. These three peaks show a low

intensity, due to electronic scattering,¹⁰ and a very broad line shape. The full width half maximum (FWHM) of D (FWHM(D)) is 127 cm^{-1} , while FWHM(G) is 79 cm^{-1} . The FWHM(G) always increase with disorder and, indeed, it is much larger than pristine graphene (FWHM(G) $< 20\text{ cm}^{-1}$)⁸ and edge-defected graphene flakes (FWHM(G) $\sim 25\text{ cm}^{-1}$).¹⁰ The high intensity ratio between the intensity of D and G (I_D/I_G) (~ 0.86) and the large FWHM(D) ($\sim 125\text{ cm}^{-1}$) is due to the presence of both structural defects (due to oxidation process) and covalent bonds (*e.g.*, C–H, C–O), both contributing to the D peak. In the case of the RGO flakes, the D and G peaks are located at 1352 cm^{-1} and 1597 cm^{-1} , respectively, while FWHM(G) and FWHM(D) are 64 cm^{-1} and 83 cm^{-1} , respectively. The softening of the G band compared to that of GO flakes could be ascribed to the presence of defected regions as consequence of thermal stresses upon annealing.¹¹ FWHM(D) and FWHM(G) are narrower compared to those of GO flakes, indicating a restoration of the sp^2 rings.⁷ The I_D/I_G for RGO (~ 1.25) is considerably higher than that of GO flakes (~ 0.86). In fact, I_G is constant as a function of disorder because is related to the relative motion of sp^2 carbons,⁷ while an increase of I_D is directly linked to the presence of sp^2 rings.^{7,8} Thus, an increase of the I_D/I_G means the restoration of sp^2 rings.⁷ For f-RGO flakes, FWHM(D) and FWHM(G) are further reduced compared to those of the RGO flakes, which means that the sp^2 rings are preserved.⁷ The I_D/I_G decreases compared to both those of GO and RGO flakes. This effect can be ascribed to the edge/defect passivation of RGO flakes after the functionalization process.^{7,8}

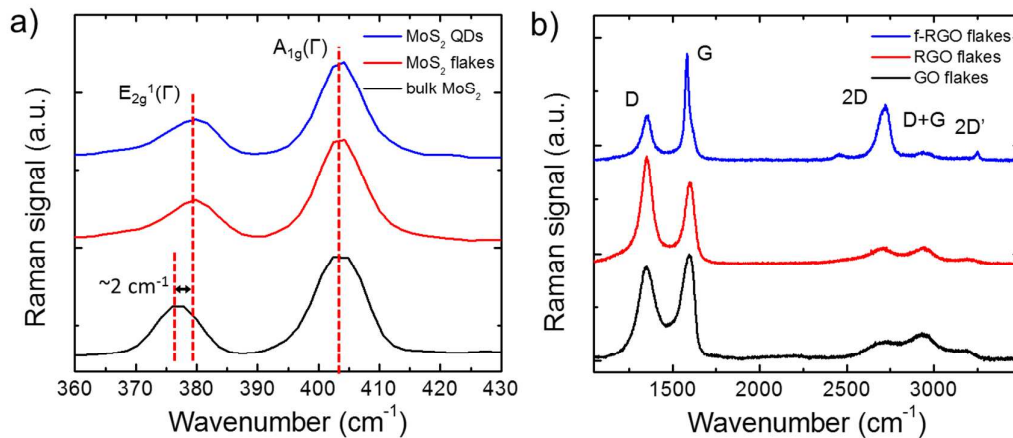


Figure S3. Raman spectra: (a) bulk MoS₂, MoS₂ flakes and MoS₂ QDs; (b) GO flakes, RGO flakes and f-RGO flakes.

Fourier-transform infrared spectroscopy analysis

Fourier-transform infrared (FTIR) spectroscopy was performed on (3-mercaptopropyl)trimethoxysilane (MPTS), RGO, f-RGO, and MoS₂ QDs:f-RGO (**Figure S4**). From the FTIR spectrum of MPTS (**Figure S4a**), it is possible to identify the bands corresponding to Si-O-Si stretching (1089 cm⁻¹), S-H stretching (2564 cm⁻¹) and C-H stretching (2830/2944 cm⁻¹). In agreement with the Scheme 1 of the main text, the first step of the process was the MPTS functionalization of the RGO flakes. As result in the FTIR spectrum of the RGO appeared a broad Si-O-Si stretching band at 1078 cm⁻¹ superimposed to the RGO FTIR spectrum (Figure S4b,c). This observation confirms the hydrolyzation and condensation between the oxygen functionalities of the RGO and the alkoxy silane groups (-OCH₃) during the MPTS functionalization.¹²⁻¹⁴ Notably, the weak peak related to the S-H bond is only shown in the FTIR spectrum of the pure MPTS. This agrees with other studies on the silane functionalization of oxide nanoparticles.¹⁵ In the FTIR spectrum of the MoS₂ QDs:f-RGO, the broad Si-O-Si stretching band of the f-RGO is still at 1078 cm⁻¹. This indicates that the hybridization did not alter the MPTS functionalization of the RGO and, at the same time, that the interaction between MoS₂ QDs and f-RGO only took place at the free SH groups of the MPTS.

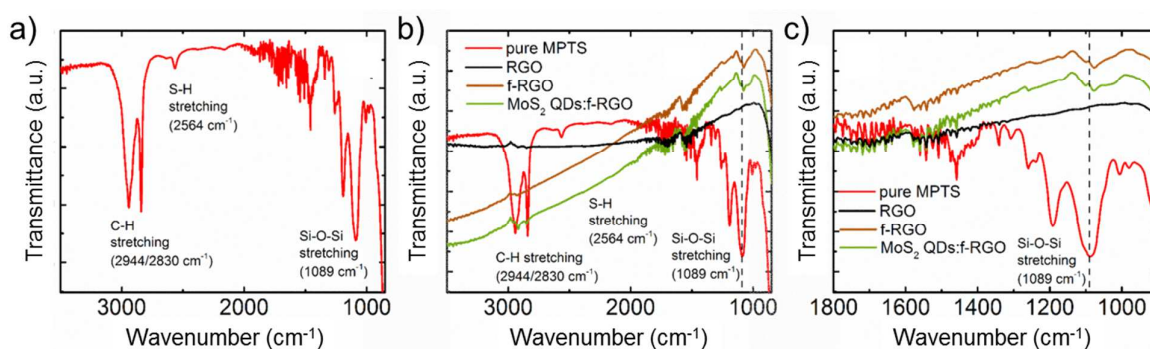


Figure S4. (a) FTIR spectrum of the pure MPTS indicating the main characteristic features: Si-O-Si, S-H and C-H stretching vibrations. (b) Comparison of the FTIR spectra corresponding to pure MPTS, RGO, f-RGO and MoS₂ QDs:f-RGO materials. (c) Corresponding zoom in the Si-O-Si area for the spectra shown in (b).

Gravitational sedimentation of the RGO and f-RGO dispersion in ethanol

Figure S5 shows photographs of 1 mg mL^{-1} RGO and f-RGO dispersions in ethanol (EtOH) after 2 h of gravitational sedimentation. The photographs show a clear sedimentation of the dispersion of RGO due to the poor hydrogen-bonding capability of the as-produced material. After the functionalization of the RGO, the presence of MPTS groups decreased the surface energy of the flakes, making f-RGO compatible with polar solvent, such as EtOH. Consequently, no significant gravitational sedimentation for f-RGO dispersions in EtOH was observed in the same timeframe.



Figure S5. Photograph of 1 mg mL^{-1} RGO and f-RGO dispersions in EtOH after 2 h of gravitational sedimentation.

Photoluminescence analysis of MoS₂ QDs

Figure S6 reports the photoluminescence (PL) spectra of MoS₂ QDs dispersion in 2-Propanol (IPA), collected at different excitation wavelengths (from 300 to 500 nm). The PL peaks were red-shifted with the increase of the excitation wavelength. This excitation-dependent PL emission can be ascribed to quantum confinement and edge state emission effect.¹⁸⁻²⁰ The sharp small features observed in the spectra were related to the IPA solvent, as proved by blank PL spectrum (inset to Figure S6).

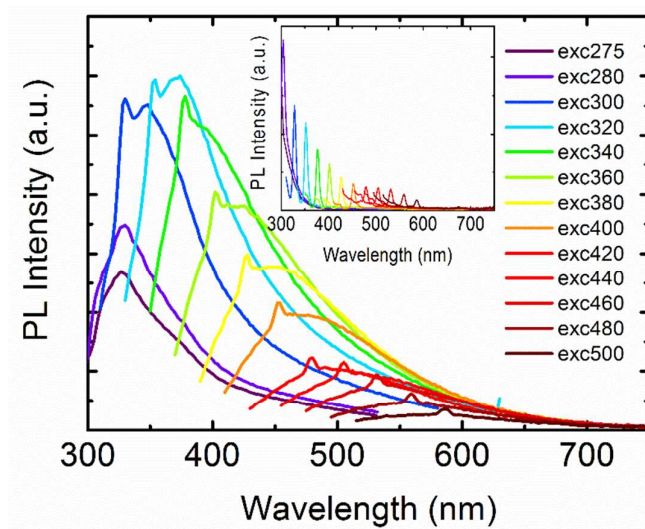


Figure S6. Photoluminescence spectra of the MoS₂ QDs at different excitation wavelength, ranging from 300 to 500 nm. The inset shows the blank (control) PL spectra of IPA at different excitation wavelengths.

Supplementary Tauc analysis of MoS₂ QDs

As commented in the main text, the Tauc plot analysis of nanocrystals can be trivial and the E_g values of MoS₂ QDs calculated by Tauc analysis has to be considered qualitatively.²¹ Previous work suggested to correct the Tauc relation for direct-allowed transition in nanocrystals by assuming the power factor (n) equal to 1.²¹ **Figure S7** reports the Tauc plot for $n = 1$, which the E_g values to be estimated at ~ 3.2 eV.

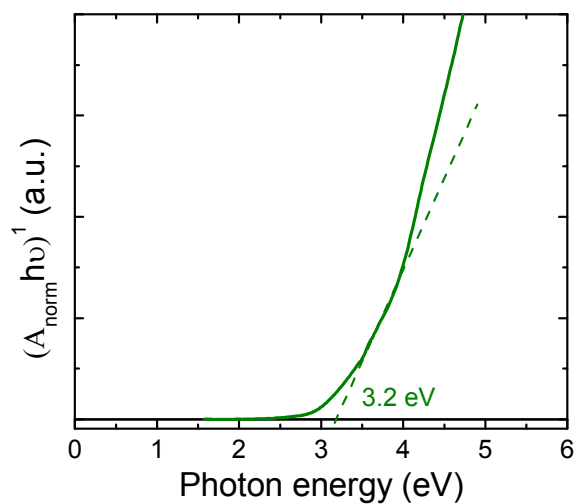


Figure S7. Tauc plot of MoS₂ QDs with $n = 1$.

Energy-dispersive X-ray spectroscopy of the MAPbI₃/MoS₂ QDs:f-RGO

Scanning electron microscopy combined with energy-dispersive X-ray spectroscopy (SEM/EDX) was carried out in order to gain insight into the coverage of the mesoscopic methylammonium lead iodide (CH₃NH₃PbI₃) perovskite (MAPbI₃) layer with MoS₂ QDs and f-RGO (**Figure S8a-c**) by preparing the perovskite solar cells (PSCs) as detailed in the Experimental Section (main text) up to the layer object of study. By analyzing the Pb (M, 2.34 keV), Mo (L α , 2.29 keV) and C (K α , 0.28 keV) peak signals by INCA[®] software (XPP matrix correction routine, which considers the atomic number and absorption effects for a standardless estimation of the composition), we confirmed the presence of MoS₂ QDs and f-RGO on the PSCs layer stack (Figure S8d-h). For the careful interpretation of the EDX data, it is important to note that (i) MAPbI₃ is already giving a C signal corresponding to the CH₃NH₃ and (ii) the Pb and Mo signals almost overlap making difficult to discern both components. Moreover, since the spiro-OMeTAD could also contribute to the C signal, we suppressed this layer in the preparation of the devices for these SEM/EDX measurements. As a control, we also determined the I/Pb atomic ratio (I (L α , 3.94 keV)) in all the samples. In this way, we obtained by evaluating at least 5 areas of about 12 \times 12 μm^2 in two samples of each type of PSC values of C/Pb = 2.2 \pm 0.1 and I/Pb = 3.0 \pm 0.1 (for the reference MAPbI₃, Figure S8d); C/Pb = 16 \pm 2 and I/Pb = 3.0 \pm 0.1 (for f-RGO/MAPbI₃, Figure S7e); C/(Pb+Mo) = 2.3 \pm 0.2 and I/Pb = 3.0 \pm 0.1 (for MoS₂ QDs/MAPbI₃, Figure S7f) and C/(Pb+Mo) = 15 \pm 2 and I/Pb = 3.1 \pm 0.1 (for MoS₂ QDs:f-RGO/MAPbI₃, Figure S8g-h). These results show that the presence of f-RGO promotes the increase of the C/Pb ratio, while the I/Pb stoichiometry (3:1) of the perovskite is preserved.

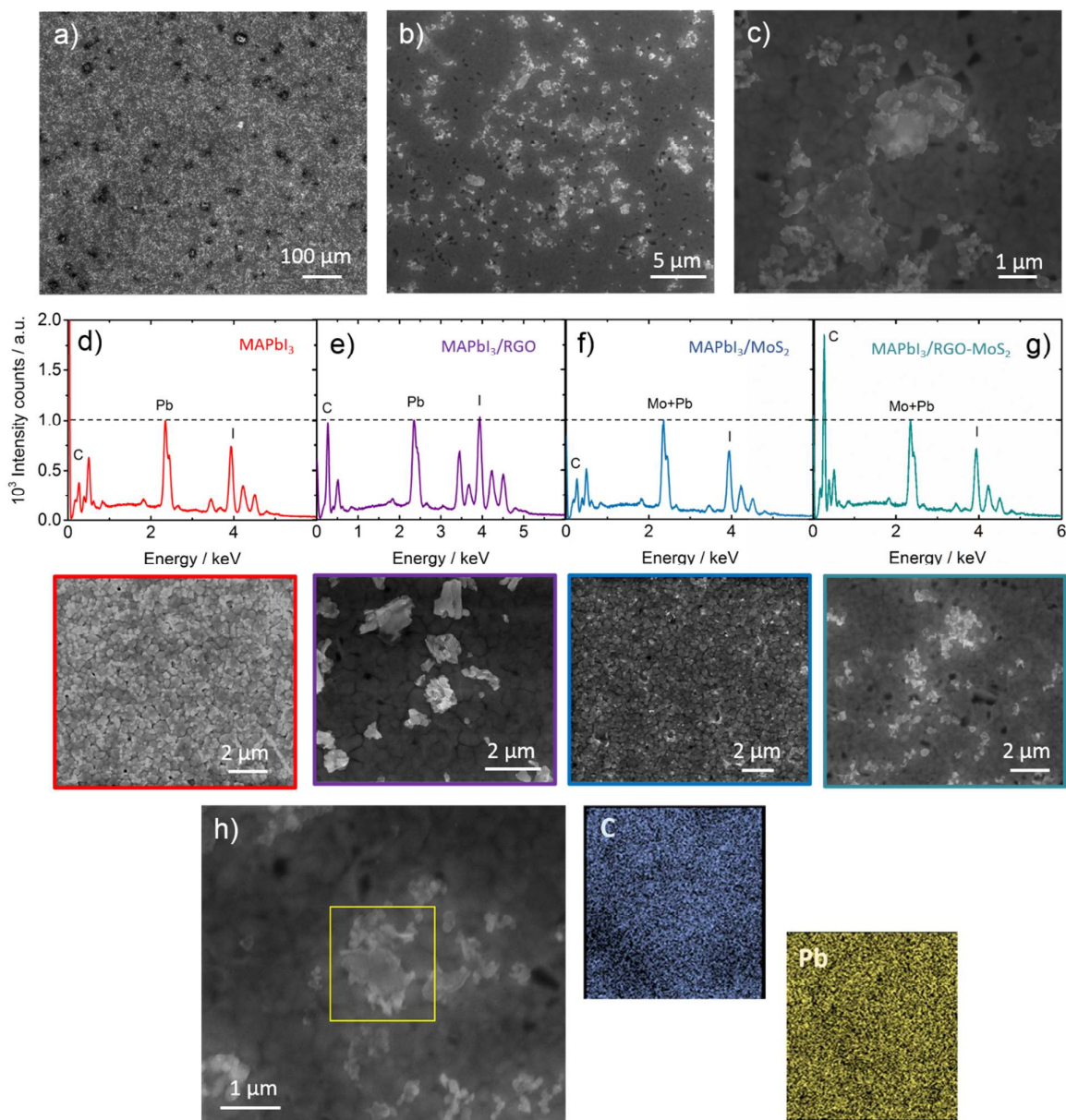


Figure S8. (a-c) Representative SEM images at different magnifications for the MoS₂ QDs:f-RGO/MAPbI₃ sample showing the coverage of the perovskite layer. Representative EDX spectra collected in areas of about 12x12 μm² for: (d) the reference MAPbI₃, (e) f-RGO/MAPbI₃, (f) MoS₂ QDs/MAPbI₃ and (g) MoS₂ QDs:f-RGO/MAPbI₃ normalized to the Pb signal accompanied of detailed SEM images. (h) A representative SEM/EDX mapping example for a small area (2x2 μm²) of MoS₂ QDs:f-RGO/MAPbI₃ sample pointed out in a yellow square.

Optical absorption spectroscopy measurements of PSCs

Figure S9 shows the UV-VIS absorption spectra of the different PSC architectures before the Au contact deposition. These results evidenced that the optical absorption of the MoS₂ QDs:f-RGO-based PSCs did not show significant differences compared to that of MoS₂ QDs-based PSC, and exhibited an increase by only ~3% and ~8% compared to that of f-RGO-based and reference PSCs. On the basis of these results, the enhanced J_{sc} value obtained with the use of f-RGO and MoS₂ QDs:f-RGO compared to that of reference device and the one of the device based on MoS₂ QDs can be attributed to the efficient charge collection in presence of f-RGO and MoS₂ QDs:f-RGO, respectively.

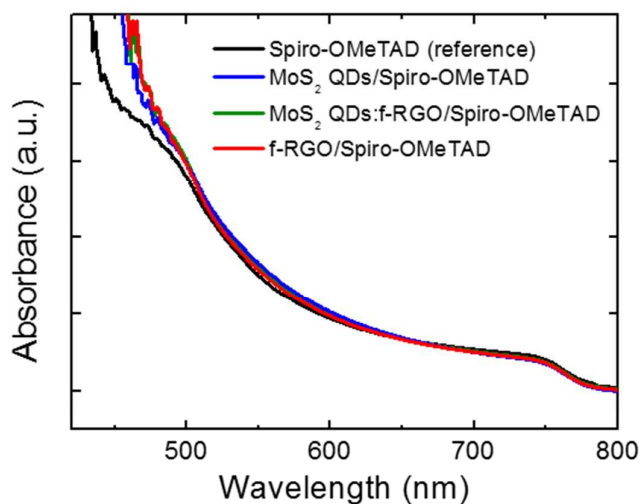


Figure S9. Absorption spectra of different PSCs before Au deposition.

Stabilized power conversion efficiency measurements

Figure S10 shows the stabilized power conversion efficiency (PCE) measurement performed with maximum power point (MPP) tracking on PSCs based on MoS₂ QDs, f-RGO and MoS₂ QDs:f-RGO as active buffer layer (ABL). The comparison with the measurement performed on reference ABL-free PSC based on solely spiro-OMeTAD as hole transport layer (HTL) is also shown. The results confirmed that the presence of MoS₂ QDs:f-RGO, as well as the f-RGO, enhance the performance of reference PSC. These results are in agreement with the I-V curve measurements of the various PSCs and the corresponding statistical analysis of the main PV parameters reported in the main text (Figure 5b and Figure 6, respectively).

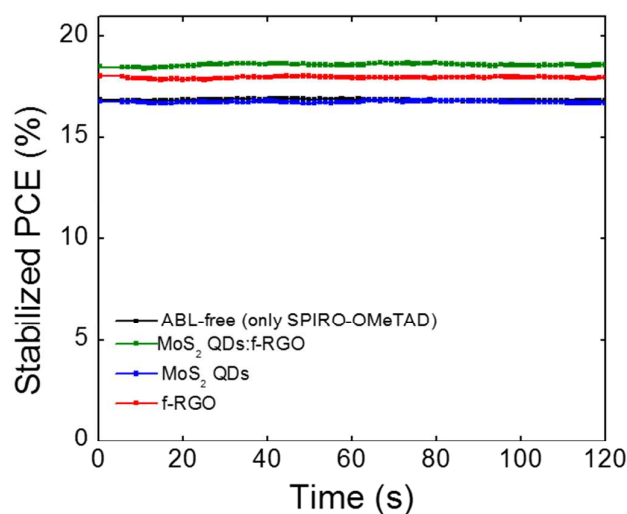


Figure S10. Stabilized PCE measurements performed with MPP tracking of the various PSCs based on MoS₂ QDs, f-RGO and MoS₂ QDs:f-RGO as ABL. The comparison with the measurement performed on reference ABL-free PSC based on exclusively spiro-OMeTAD as HTL is also shown

Hysteresis analysis

Figure S11 reports the forward and reverse I-V curves for the PSCs based MoS₂ QDs, f-RGO and MoS₂ QDs:f-RGO as ABLs. The comparison with the measurements performed on reference ABL-free PSC based on solely spiro-OMeTAD as HTL is also shown. Clearly, the presence of MoS₂ QDs:f-RGO as ABLs, in addition to increase the PCE, also decreases the hysteresis phenomena compared to those of reference PSCs and the other ABL-based devices.

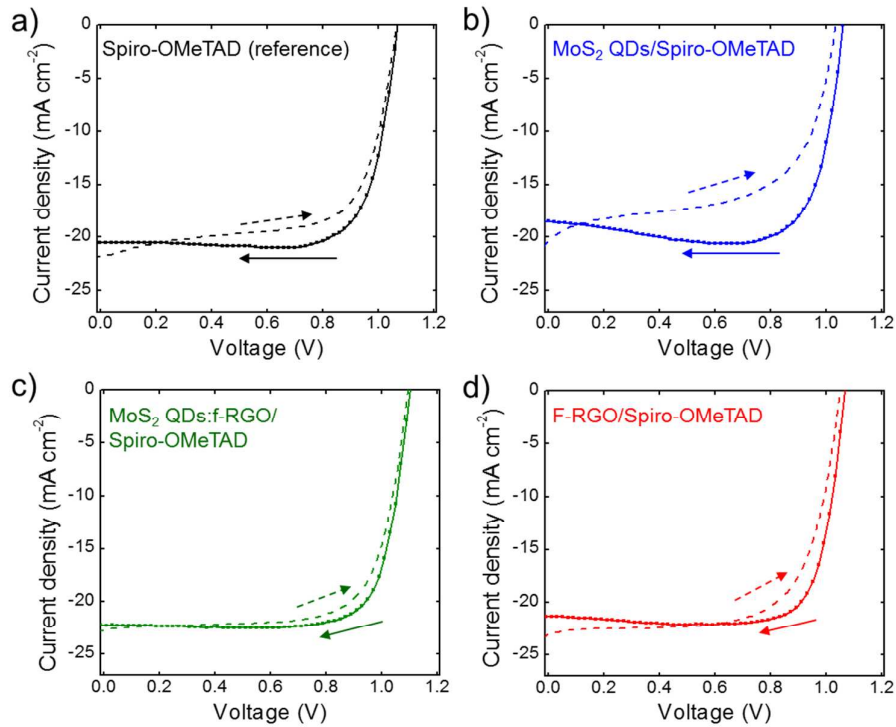


Figure S11. Forward and reverse I-V curves for the PSCs based on (a) solely spiro-OMeTAD (reference), (b) spiro-OMeTAD/MoS₂ QDs, (c) spiro-OMeTAD/MoS₂ QDs:f-RGO and (d) spiro-OMeTAD/f-RGO.

Spray coating parameter optimization for MoS₂ QDs, f-RGO and MoS₂ QDs:f-RGO film deposition

The spray coating deposition of MoS₂ QDs, f-RGO and MoS₂ QDs:f-RGO dispersion in IPA onto MAPbI₃ surface could degrade the native properties of the latter. In order to retain the optical properties of MAPbI₃, the spray coating was carried out by using N₂ as inert flowing gas, and the deposition parameters (N₂ pressure (P_{N2}), nozzle aperture (AP_{nozzle}), nozzle distance (d_{nozzle}), temperature of substrate (T_{sub}), spray velocity (v_{spray}), and flow rate of solution (FR_{solution})) were optimized by monitoring their influence on the UV-Vis absorption spectrum of MAPbI₃ substrates. The degradation of the perovskite was quantified by the relative optical absorption loss, *i.e.*, the module of ratio between the difference of its optical absorption before (Abs₀) and after (Abs_{spray}) material spray coating referred to Abs₀ (in formula: |(Abs₀-Abs_{spray})/Abs₀|).

Figure S12a shows the degradation (average values calculated in the ranges of 420-600 nm and 700-780 nm) measured by varying the most critical spray coating parameters and adopting d_{nozzle} = 9 cm, v_{spray} = 300mm s⁻¹, FR_{solution} = 20%. The best parameters were found to be: P_{N2} = 1 bar, AP_{nozzle} = 0.6 mm, d_{nozzle} = 9 cm, T_{sub} = 80 °C, v_{spray} = 300mm s⁻¹, and a FR_{solution} = 20%. The corresponding degradation of MAPbI₃ film was less than 2% (Figure S12b).

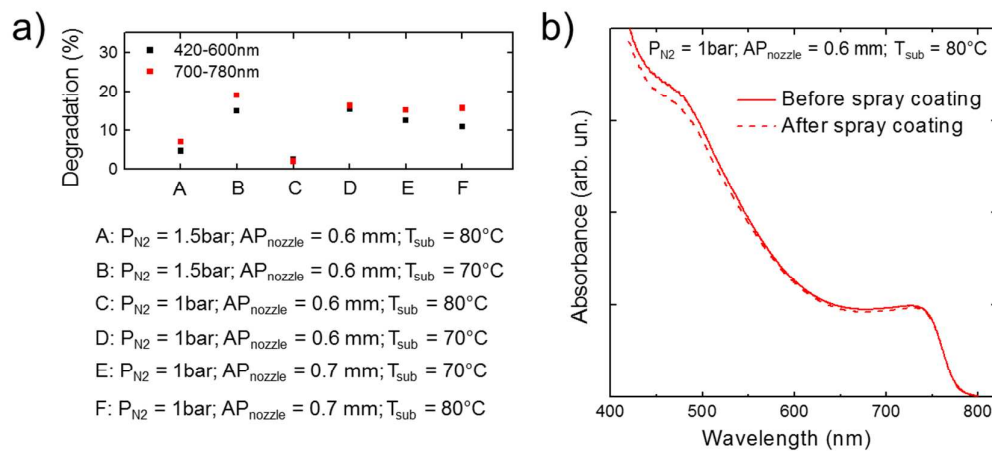


Figure S12. a) Sketch of the degradation of MAPbI₃ as a function of spray coating settings. b) Absorbance of MAPbI₃ before and after spray coating of IPA with optimized parameter setting denoted as C in panel a: P_{N2} = 1 bar, AP_{nozzle} = 0.6 mm, d_{nozzle} = 9 cm, T_{sub} = 80 °C, v_{spray} = 300mm s⁻¹, and a FR_{solution} = 20%.

REFERENCES

- (1) Mak, K. F.; Lee, C.; Hone, J.; Shan, J.; Heinz, T. F. Atomically Thin MoS₂: A New Direct-Gap Semiconductor. *Phys. Rev. Lett.* **2010**, *105* (13), 136805.
- (2) Lee, C.; Yan, H.; Brus, L. E.; Heinz, T. F.; Hone, J.; Ryu, S. Anomalous Lattice Vibrations of Single- and Few-Layer MoS₂. *ACS Nano* **2010**, *4* (5), 2695–2700.
- (3) Huang, Y.; Wu, J.; Hwang, K. C. Thickness of Graphene and Single-Wall Carbon Nanotubes. *Phys. Rev. B* **2006**, *74* (24), 245413.
- (4) Novoselov, K. S.; Geim, A. K.; Morozov, S. V.; Jiang, D.; Zhang, Y.; Dubonos, S. V.; Grigorieva, I. V.; Firsov, A. A. Electric Field Effect in Atomically Thin Carbon Films. *Science* **2004**, *306* (5696), 666–669.
- (5) Saito, R.; Tatsumi, Y.; Huang, S.; Ling, X.; Dresselhaus, M.S. Raman Spectroscopy of Transition Metal Dichalcogenides. *J. Phys. Condens. Matter* **2016**, *28* (35), 353002.
- (6) Bellani, S.; Najafi, L.; Capasso, A.; Del Rio Castillo, A. E.; Antognazza, M. R.; Bonaccorso, F. Few-Layer MoS₂ Flakes as a Hole-Selective Layer for Solution-Processed Hybrid Organic Hydrogen-Evolving Photocathodes. *J. Mater. Chem. A* **2017**, *5* (9), 4384–4396.
- (7) Ferrari, A. C.; Basko, D. M. Raman Spectroscopy as a Versatile Tool for Studying the Properties of Graphene. *Nat. Nanotechnol.* **2013**, *8*, 235.
- (8) Ferrari, A. C.; Meyer, J. C.; Scardaci, V.; Casiraghi, C.; Lazzeri, M.; Mauri, F.; Piscanec, S.; Jiang, D.; Novoselov, K. S.; Roth, S.; *et al.* Raman Spectrum of Graphene and Graphene Layers. *Phys. Rev. Lett.* **2006**, *97* (18), 187401.
- (9) Su, C.-Y.; Xu, Y.; Zhang, W.; Zhao, J.; Tang, X.; Tsai, C.-H.; Li, L.-J. Electrical and Spectroscopic Characterizations of Ultra-Large Reduced Graphene Oxide Monolayers. *Chem. Mater.* **2009**, *21* (23), 5674–5680.
- (10) Maragó, O. M.; Bonaccorso, F.; Saija, R.; Privitera, G.; Gucciardi, P. G.; Iati, M. A.; Calogero, G.;

- Jones, P. H.; Borghese, F.; Denti, P.; *et al.* Brownian Motion of Graphene. *ACS Nano* **2010**, *4* (12), 7515–7523.
- (11) Wang, P.; Liu, Z.-G.; Chen, X.; Meng, F.-L.; Liu, J.-H.; Huang, X.-J. UV Irradiation Synthesis of an Au–graphene Nanocomposite with Enhanced Electrochemical Sensing Properties. *J. Mater. Chem. A* **2013**, *1* (32), 9189–9195.
- (12) Hou, S.; Su, S.; Kasner, M. L.; Shah, P.; Patel, K.; Madarang, C. J. Formation of Highly Stable Dispersions of Silane-Functionalized Reduced Graphene Oxide. *Chem. Phys. Lett.* **2010**, *501* (1), 68–74.
- (13) Yao, H.; Jin, L.; Sue, H.-J.; Sumi, Y.; Nishimura, R. Facile Decoration of Au Nanoparticles on Reduced Graphene Oxide Surfaces *via* a One-Step Chemical Functionalization Approach. *J. Mater. Chem. A* **2013**, *1* (36), 10783.
- (14) Martin-Garcia, B.; Polovitsyn, A.; Prato, M.; Moreels, I. Efficient Charge Transfer in Solution-Processed PbS Quantum Dot-Reduced Graphene Oxide Hybrid Materials. *J. Mater. Chem. C* **2015**, *3* (27), 7088–7095.
- (15) Villa, S.; Riani, P.; Locardi, F.; Canepa, F. Functionalization of Fe₃O₄ NPs by Silanization: Use of Amine (APTES) and Thiol (MPTMS) Silanes and Their Physical Characterization. *Materials (Basel)*. **2016**, *9* (10), 826.
- (16) Willis, L. J.; Loehr, T. M.; Miller, K. F.; Bruce, A. E.; Stiefel, E. I. Raman and Infrared Spectroscopic Studies of Dioxomolybdenum(VI) Complexes with Cysteamine Chelates. *Inorg. Chem.* **1986**, *25* (23), 4289–4293.
- (17) Nagaraju, G.; Tharamani, C. N.; Chandrappa, G. T.; Livage, J. Hydrothermal Synthesis of Amorphous MoS₂ Nanofiber Bundles *via* Acidification of Ammonium Heptamolybdate Tetrahydrate. *Nanoscale Res. Lett.* **2007**, *2* (9), 461–468.
- (18) Gan, Z. X.; Liu, L. Z.; Wu, H. Y.; Hao, Y. L.; Shan, Y.; Wu, X. L.; Chu, P. K. Quantum Confinement

Effects across Two-Dimensional Planes in MoS₂ Quantum Dots. *Appl. Phys. Lett.* **2015**, *106* (23), 233113.

- (19) Gan, Z.; Xu, H.; Hao, Y. Mechanism for Excitation-Dependent Photoluminescence from Graphene Quantum Dots and Other Graphene Oxide Derivates: Consensus, Debates and Challenges. *Nanoscale* **2016**, *8* (15), 7794–7807.
- (20) Gopalakrishnan, D.; Damien, D.; Li, B.; Gullappalli, H.; Pillai, V. K.; Ajayan, P. M.; Shaijumon, M. M. Electrochemical Synthesis of Luminescent MoS₂ Quantum Dots. *Chem. Commun.* **2015**, *51* (29), 6293–6296.
- (21) Feng, Y.; Lin, S.; Huang, S.; Shrestha, S.; Conibeer, G. Can Tauc Plot Extrapolation Be Used for Direct-Band-Gap Semiconductor Nanocrystals? *J. Appl. Phys.* **2015**, *117* (12), 125701.